Applied Catalysis B: Environment and Energy 362 (2025) 124709

Contents lists available at ScienceDirect

Applied Catalysis B: Environment and Energy

journal homepage: www.elsevier.com/locate/apcatb

Built-in electric field-driven electron transfer behavior at Ru-RuP_2 heterointerface fosters efficient and CO-resilient alkaline hydrogen oxidation

Yi Liu [a], Lianrui Cheng [a], Shuqing Zhou [a], Chenggong Niu [a], Tayirjan Taylor Isimjan [b,*], Xiulin Yang [a,*]

[a] Guangxi Key Laboratory of Low Carbon Energy Materials, School of Chemistry and Pharmaceutical Sciences, Guangxi Normal University, Guilin, Guangxi 541004, China

[b] Saudi Arabia Basic Industries Corporation (SABIC) at King Abdullah University of Science and Technology (KAUST), Thuwal 23955-6900, Saudi Arabia

ARTICLE INFO

Keywords:
Heterostructure
Hydrogen oxidation reaction
CO-resilient
Asymmetric charge distribution
Built-in electric field

ABSTRACT

Exploiting a cost-effective electrocatalyst for hydrogen oxidation reaction (HOR) with high-performance and CO poisoning resistance is essential for the widespread application of alkaline anion exchange membrane fuel cells (AEMFCs). Herein, we craft a unique Ru-RuP_2 heterostructure within hollow mesoporous carbon sphere (Ru-RuP_2@C) using phosphide-controlled phase-transition approach. Benefiting from the interfacial electron transfer from RuP_2 to Ru, the Ru-RuP_2@C electrocatalyst exhibits impressive HOR performance with a mass activity of 2.87 mA μg_{Ru}^{-1}. Notably, Ru-RuP_2@C demonstrates strong tolerance to 1000 ppm CO, a capability lacking in PtRu/C and Pt/C. When serves as an anode catalyst for AEMFC, it achieves a peak power density of 521 mW cm^{-2}, comparable to Pt/C. Experimental and theoretical analyses reveal that the built-in electric field, resulting from work function differences, creates an asymmetric charge distribution that modulates the *d*-band center of Ru-RuP_2@C. This optimizes the adsorption strength of hydrogen and hydroxide intermediates, thereby accelerating HOR catalytic kinetics.

1. Introduction

Hydrogen (H_2) energy is highlighted as a competitive alternative to fossil fuels due to its high energy density and pollution-free combustion products, effectively alleviating the global energy and environmental crisis [1,2]. Hydrogen-oxygen fuel cells (HOFCs), a promising energy conversion devices with zero-carbon emission, show great prospect for civilian applications [3]. Despite the current prevalence of proton exchange membrane fuel cells (PEMFCs), the rapid development of anion exchange membranes and non-precious metal oxygen reduction (ORR) catalysts, along with the limitations of PEMFCs requiring a large number of platinum-based catalysts for both cathode and anodes, have increasingly attracted industrial and research attention towards the application potential of AEMFCs [4,5]. Nevertheless, to achieve performance comparable to PEMFCs, AEMFCs require not only superior ORR catalysts and anion exchange membranes, but also anode HOR catalysts that match the standards of the most advanced platinum-based HOR catalysts, offering advantages such as low cost and resistance to CO poisoning [6,7]. Unfortunately, when the electrolyte shifts from acidic to alkaline, even the state-of-the-art Pt-based catalysts experience a reduction in HOR kinetics by two to three orders of magnitude, leading to a sharp increase in the use of noble metals [8,9]. Therefore, developing cost-effective alkaline HOR catalysts with high activity and resistance to CO poisoning is paramount for advancing AEMFCs.

The adsorption of hydrogen (H_{ad}) and hydroxyl (OH_{ad}) are key metrics for describing alkaline HOR performance, with their adsorption strength being closely related to the activity of the electrocatalysts [10,11]. Researchers have found that ruthenium (Ru) possesses reasonable oxygenophilicity and a hydrogen binding energy (HBE) comparable to Pt, along with tremendous cost-effectiveness than Pt, positioning it as a potential alternative to Pt as an alkaline HOR catalyst [12,13]. However, a single Ru catalyst suffers from inherent super HBE and insufficient hydroxyl adsorption energy under alkaline conditions, resulting in retarded HOR kinetics. Thus, multiple strategies have been exploited to fine-tune the adsorption strength of intermediate, such as incorporating heteroatom [14], crafting specialized structures [15], and adjusting the

* Corresponding authors.
E-mail addresses: isimjant@sabic.com (T.T. Isimjan), xlyang@gxnu.edu.cn (X. Yang).

https://doi.org/10.1016/j.apcatb.2024.124709
Received 27 June 2024; Received in revised form 1 October 2024; Accepted 14 October 2024
Available online 16 October 2024

support [13], all aimed at achieving exceptional electrocatalytic outcomes. Recent studies have demonstrated that constructing a built-in electric field (BEF) within heterogeneous materials can accelerate the rate-determining Volmer step by promoting hydrogen adsorption in the electron-rich region and hydroxyl adsorption in the electron-deficient region during the HOR process [16]. Specifically, the BEF, formed due to differences in work functions between materials, can drive interfacial charge redistribution through electron transfer. This process manipulates the *d*-band structure, thereby optimizing the intermediate adsorption energies and accelerating catalytic reaction kinetics [17], as demonstrated in systems such as Ru-RuO_2/C [18]; Ni_2P-CoCH/CFP [19]; and Ni/V_2O_3 [16].

In recent years, noble transition metal phosphides (TMPs) have attracted significant attention in catalysis due to their functional diversity and high catalytic activity. For instance, Huang et al. developed a RuP@RuP_2 core-shell structure via a phosphorating-controlled phase transformation strategy, which enhanced electron transfer from the RuP core to the RuP_2 shell, optimizing *H adsorption free energy and improving HER/HOR catalytic efficiency [20]. Luo et al. designed a series of ruthenium phosphides as model catalysts and systematically investigated the volcanic relationship between phosphorus content and alkaline HOR activity [21]. However, there is a lack of research on constructing a built-in electric field in RuP_x-based catalysts to tune the *d*-band center. Moreover, RuP_x catalysts with both high HOR activity and strong CO tolerance are particularly rare. Given this context, manipulating the *d*-band center through BEF formation to optimize the adsorption energies of hydrogen/hydroxyl and *CO intermediates presents a promising strategy for developing efficient and CO-tolerant RuP_x-based catalysts for HOR catalysis.

Herein, we successfully created a porous Ru/RuP_2 heterojunction hollow nanosphere (denoted as Ru-RuP_2@C) with abundant interfaces for efficient HOR through simple phosphorization strategy. Spectroscopic analyses coupled with density functional theory (DFT) calculations unveiled that the variation in work functions between Ru and RuP_2 generated a built-in electric field, driving electron migration from RuP_2 to Ru at the Ru-RuP_2 heterointerface. These dynamics resulted in an asymmetrical charge distribution and a consequential shift in the *d*-band center, optimally adjusting the adsorbed strength of intermediates and lowering the reaction energy barrier during the HOR process. As anticipated, the synthesized Ru-RuP_2@C showcased exceptional catalytic performance in alkaline electrolyte, boasting mass activity and exchange current density of 2.87 mA μg_{Ru}^{-1} and 2.73 mA cm^{-2}, respectively. Additionally, the Ru-RuP_2@C maintained minimal current decay even in 1000 ppm CO, underscoring its impressive anti-CO poisoning capacity. When further utilized as an anode catalyst for AEMFC, a peak power density of 521 mW cm^{-2} was acquired.

2. Experimental section

2.1. Chemicals

All chemicals and reagents were used as received without any additional purification. These comprised of tetraethyl silicate (TEOS, ≥28.0 %, Aladdin, 500 mL), ammonia solution ($NH_3{\cdot}H_2O$, 25.0 %—28.0 % Xilong Science, 500 mL), 3-hydroxytyramine hydrochloride ($C_8H_{11}NO_2{\cdot}HCl$, ≥98 %, Aladdin, 25 g), ruthenium acetylacetonate ($C_{15}H_{21}O_6Ru$, 99.95, Aladdin, 25 g), sodium hypophosphite monohydrate ($NaH_2PO_2{\cdot}H_2O$, ≥99 %, Xilong Science, 500 g), ascorbic acid (AA, >99.0 %, Aladdin, 100 g), ethanol absolute (AR, 99.5 %, Xilong Science, 500 mL), commercial Pt/C (20 wt% Pt, Alfa Aesar, 1 g), nafion solution (5 wt%, Alfa Aesar, 100 mL), and potassium hydroxide (KOH, AR, >90 %, Macklin, 500 g). The experiment was conducted using deionized water (18.25 MΩ cm^{-1}) from a water purification system (Ulupure).

2.2. Synthesis of hollow mesoporous carbon spheres (HMCS)

HMCS were fabricated according to our previously reported work [22]. Specifically, 5 mL of TEOS was quickly added to a solution containing 100 mL of ethanol, 30 mL of deionized water, and 5 mL of NH_4OH under vigorous stirring. After reacting for an hour, 500 mg of 3-hydroxytyramine hydrochloride was incorporated, and stirring was continued for 12 h at room temperature. The resulting black powder was collected by centrifugation, washed several times with deionized water and ethanol, and dried at 60 °C overnight. The sample was then heated to 400 °C at a heating rate of 5 °C min^{-1} under N_2 for 2 h, followed by heating to 800 °C for 3 h to obtain SiO_2 spheres. Finally, the SiO_2 was thoroughly removed using 3 M NaOH, yielding hollow mesoporous carbon spheres.

2.3. Preparation of mesoporous Ru-RuP_2@C hollow heterostructure, RuP_2@C and Ru@C

Typically, 50 mg of previously prepared HMCS support and 40 mg of ruthenium acetylacetonate were dissolved in 10 mL of water to form solution A. And 0.15 g of ascorbic acid was dissolved in 6 mL of water to form solution B. Solution B was slowly added dropwise to solution A by ultrasonication for 30 min, and the mixture was then oil-bathed at 60 °C for 9 h. The resultant precursor was collected via centrifugation, washed three times with water and ethanol, and dried in an oven at 60 °C for 12 h. Subsequently, 1 g of $NaH_2PO_2{\cdot}H_2O$ and 15 mg of precursor were placed upstream and downstream of the tube furnace, and the precursor was heated at 600 °C for 2 h, with a temperature ramp rate of 5 °C min^{-1} in an H_2/Ar mixed atmosphere. After naturally cooling, the final product was denoted as Ru-RuP_2@C, with a specific Ru content of 3.65 wt%, which was confirmed by inductively coupled plasma (ICP) measurements [7].

For comparison, the fabrication of RuP_2@C was analogous to that of Ru-RuP_2@C, except that the temperature was changed to 650 ℃, as explained in the discussion section. Concurrently, Ru@C can be synthesized without P source.

2.4. Physical characterization

Powder X-ray diffraction (XRD, Rigaku D/Max 2500 V/PC, Japan, Cu Ka radiation over the 2θ range of 10–90º) was measured to investigate the crystal structure and phase composition of samples. Scanning electron microscopy (SEM, FEI Quanta 200 FEG) and transmission electron microscopy (TEM, JEM-2100 F) were recorded to characterize the morphology and elemental distribution of the catalysts. The chemical state and electronic structure of the samples were analyzed by X-ray photoelectron spectroscopy (XPS, JPS-9010 Mg Kα). Metal contents in the catalysts were examined using inductively coupled plasma mass spectroscopy (ICP-MS, PerkinElmer corporation, FLexar-NexION300X). The specific BET surface area (Brunauer–Emmett–Teller) and pore size distribution of the samples were used to measure the specific surface area and pore size distribution, respectively. Raman spectra were obtained using a Renishaw in Via with a visible laser (λ = 532 nm). Ultraviolet photoelectron spectroscopy (UPS) was performed on X-ray photoelectron spectroscopy (PHI5000 VersaProbe III).

2.5. Electrochemical measurements

All the electrocatalytic measurements were performed in a standard three-electrode system by the CHI 760E (Shanghai, China) electrochemical analyzer. In this work, glassy carbon electrode (GCE, diameter: 5 mm, disk area: 0.196 cm^2) was chosen as the working electrode, graphite rod and saturated KCl-filled with Ag/AgCl were served as counter electrode and reference electrode, respectively. Electrochemical impedance spectroscopy (EIS) was measured using a multichannel potentiostat (Biologic VMP3) at the open circuit potential from 200 kHz

to 10 mHz. All the measured potentials were converted relative to reversible hydrogen electrode (RHE) via calibration ($E_{Ag/AgCl} + 0.197 + 0.059 \times pH$)

To fabricate a thin-film working electrode, 3 mg of sample and 5 μL of Nafion solution (5 wt%), were ultrasonically dispersed in deionized water-isopropanol solution (volume ratio,1: 1) to form a homogeneous ink. Afterwards, 10 μL well-dispersed catalyst ink was suspended onto the pre-polished glassy carbon electrode (Ru loading was 12.6 μg_{Ru} cm^{-2}), drying ink prior to measurement.

Before HOR measurements, the 0.1 M KOH electrolyte was bubbled with pure H_2 for 30 min to gain H_2 saturation. The electrodes were pre-cycled between 0 V and 1.0 V (vs. RHE) in pre-made N_2-saturated 0.1 M KOH to reach a steady state. HOR polarization curves were collected at a sweep rate of 10 mV s^{-1} ranging from −0.05 V to 0.5 V (vs. RHE) under 1600 revolutions per minute (rpm) of the rotating disk electrode (RDE) rotation rate. The accelerated degradation testing (ADT) was assessed by repeating the potential scan from 0 V to 1.0 V (vs. RHE) for 1000 cycles at the scanning rate of 100 mV s^{-1} in H_2-saturated 0.1 M KOH. Chronoamperometric characterization was performed at 50 mV vs. RHE.

CO stripping voltammetry measurements was performed by holding the potential of working electrode at 0.1 V (vs. RHE) for 10 min in the UHP CO to fully adsorb CO on the metal surface. Following, N_2 was bubbled for 40 min to completely remove residual CO in the electrolyte. CO stripping current was obtained by cycling between 0 V and 1.2 V (vs. RHE) at 0.02 V s^{-1} without any extra CO. The 1st CV is the stripping of the monolayer CO, where the CO oxidation peak can be noticed. The 2nd CV represents the background:

$$ECSA_{active\ metal} = \frac{Q_{co}}{0.42mCcm^{-2} * M}$$

where Q_{CO} is the total charge of adsorbed CO oxidation, 0.42 mC cm^{-2} corresponds to monolayer CO adsorption and M represents the total loading of active metal on the working electrode.

2.6. AEMFCs test

The synthesized Ru-RuP_2@C or Pt/C catalysts were used as the anode, loaded at 0.2 mg_{Ru} cm^{-2} and 0.4 mg_{Pt} cm^{-2}, respectively. Pt/C (HiSpec 4000, 40 wt% Pt, Alfa Aesar) served as the cathode catalyst with a loading of 0.4 mg_{Pt} cm^{-2}. To prepare the anode catalyst ink, Ru-RuP_2@C was mixed with ionomer (I-250 2 %wt IEC(Cl^-)> 2.4 mmol g^{-1}), isopropanol, and deionized water. The mixture was sonication for 2 h, then dripped onto a membrane (Alkymer W-25) to fabricate a catalyst-coated membrane (CCM). All CCMs were soaked in 3 M KOH solution for 6 h and thoroughly rinsed with deionized water

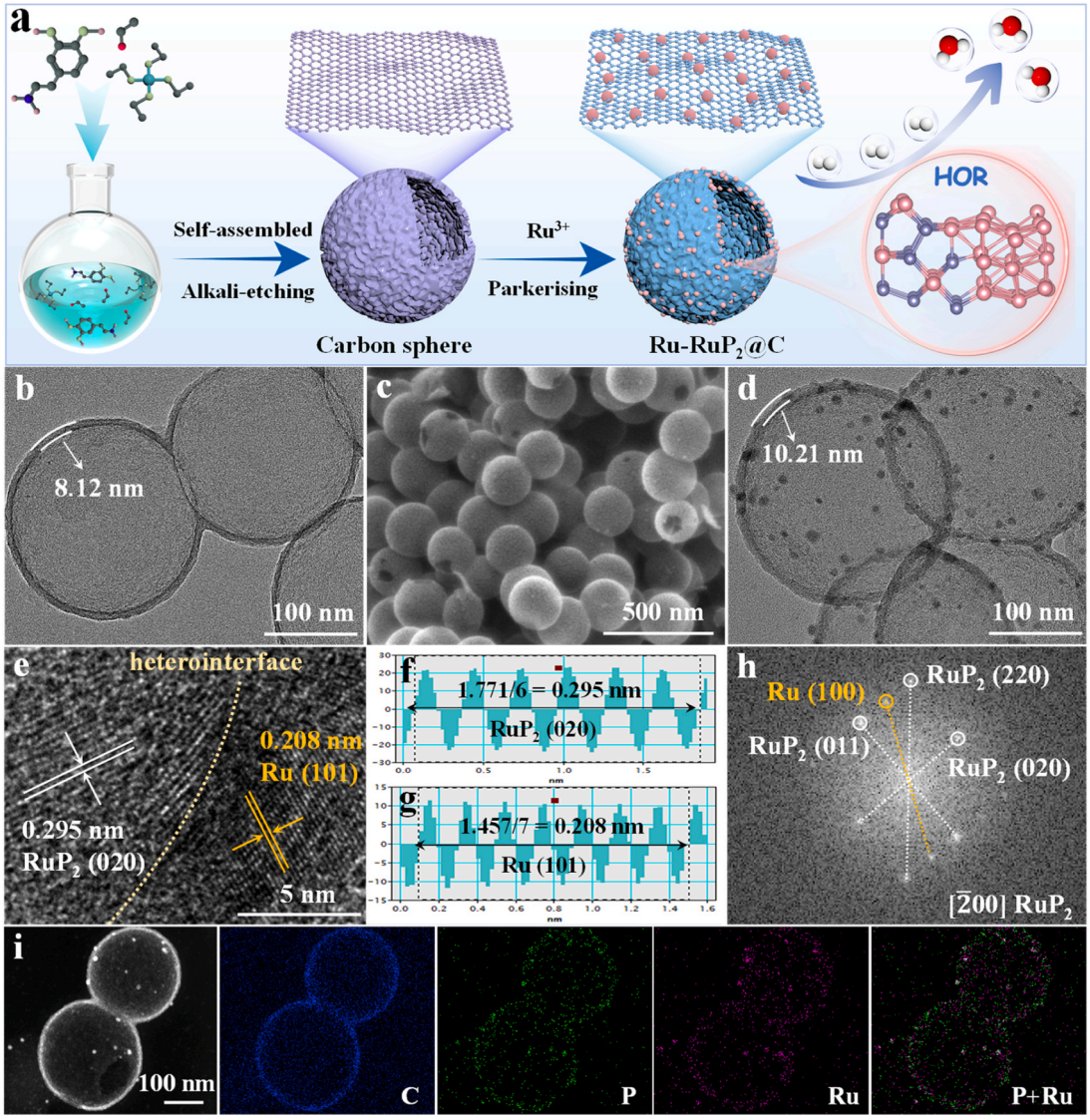

Fig. 1. (a) Schematic illustration of Ru-RuP_2@C synthesis. (b) TEM image of HMCS. (c) SEM, (d) TEM, (e-g) High-resolution TEM image and corresponding lattice spacing profiles, (h) the FFT pattern from e, and (i) HAADF-STEM mage and corresponding elemental mappings of Ru-RuP_2@C.

before assembly. Polarization curves were recorded using a fuel cell test station in current-scanning mode, with ultra-high purity H_2 and O_2 humidified at 80 °C, supplied at a flow rate of 0.5 L min^{-1} for both the anode and cathode. The cell temperature was maintained at 80 °C and the back-pressure was set at 205 kPa.

3. Results and discussion

3.1. Synthesis and structural characterization

The reaction microenvironment at the catalyst-electrolyte-hydrogen three-phase interface is crucial for enhancing the HOR catalytic capability [23]. To this end, we employed a hard template method to fabricate hollow mesoporous spherical materials that can expose abundant active sites. The design strategy of Ru-RuP_2@C was illustrated in Fig. 1a. First, pre-synthesized hollow mesoporous carbon spheres (HMCS) were ultrasonically dispersed in an aqueous solution containing a specific amount of Ru^{3+} precursor. Then, an aqueous solution with ascorbic acid was added drop-by-drop under ultrasound to reduce the Ru species entirely. Finally, the heterostructured Ru-RuP_2@C was acquired through a vacuum pyrolysis strategy with sodium hypophosphite as the phosphorus sources. Its counterparts, RuP_2@C and Ru/C, were fabricated using a similar approach. Scanning electron microscopy (SEM) and transmission electron microscopy (TEM) were utilized to gain insight into the morphological evolution of Ru-RuP_2@C [24]. As depicted in Fig. S1, SiO_2@DA presented a monodisperse spherical morphology. After removing SiO_2 through carbonization and alkali etching, the HMCS carriers displayed a hollow spherical structure with cracks, indicating the presence of porosity (Fig. S2) [25]. TEM further confirmed its hollow structure characteristics (Fig. 1b), in which the shell thickness of pure HMCS was about 8.12 nm. Figs. 1c-d indicated that the hollow spherical morphology with a rough outer shell and well-defined contours was still maintained after anchoring the Ru-RuP_2 heterojunction to HMCS, with the shell thickness increasing to 10.21 nm. The increase in wall thickness suggested that the Ru-RuP_2 heterojunction was deposited onto the carbon shell layer, with an estimated thickness of approximately 2.09 nm [26,27]. The exposed hollow porous texture of the inner and outer surfaces was expected to improve the accessibility of the active site and accelerate the mass transfer kinetics [26]. Observation of high-resolution TEM (HRTEM) image (Fig. 1e) revealed the existence of a distinct interface in the Ru-RuP_2@C sample, where the interfacial lattice fringes of 0.295 and 0.208 nm corresponded to the (020) facet of RuP_2 and the (101) facet of Ru, respectively (Figs. 1f-g). In addition, the relatively fast Fourier transform (FFT) image also showed precise Ru and RuP_2 lattices, further demonstrating the heterogeneous interface between Ru and RuP_2 in Ru-RuP_2@C (Fig. 1h). The elemental mapping analysis revealed that C was primarily concentrated in the hollow sphere shell layer, while P and Ru were uniformly distributed across the entire nanosphere structure (Fig. 1i).

Fig. 2a demonstrated the X-ray diffraction (XRD) pattern of the Ru-RuP_2@C heterogeneous electrocatalyst. Its diffraction peaks matched well with the RuP_2 (JCPDS: 71–0167) and Ru phases (JCPDS: 88–1734), further indicating the successful formation of Ru-RuP_2 heterostructure [28,29]. Then, we performed additional XRD analysis at different temperatures to verify the synthesis of the single RuP_2@C sample (Fig. 2b). The results showed that Ru diffraction peaks gradually disappeared at higher temperatures. No signs of metallic Ru diffraction peaks were

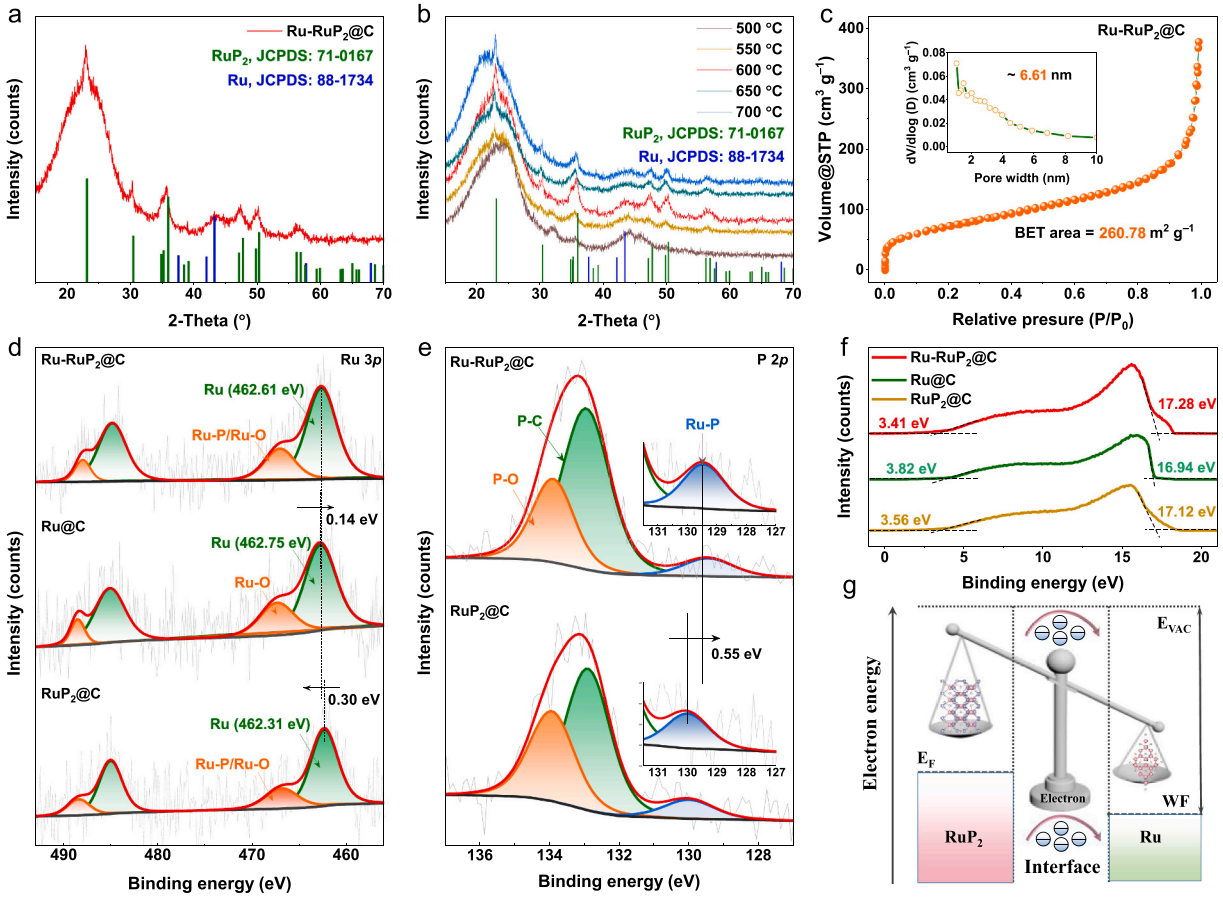

Fig. 2. (a) XRD pattern, (b) XRD patterns in different temperatures, and (c) N_2 adsorption-desorption isotherms and corresponding pore distribution curve of Ru-RuP_2@C. High-resolution (d) Ru 3*p*, and (e) P 2*p* XPS spectra for Ru-RuP_2@C, RuP_2@C, and Ru@C. (f) UPS spectra, and (g) schematic illustration of the built-in electric field and charge redistribution.

detected when temperatures were equal to or higher than 650 °C. Subsequent analysis of high-resolution images for the sample pyrolyzed at 650 °C (Fig. S3) manifested that the lattice fringes were exclusively from RuP_2, with no lattice fringes of metallic Ru observed. Consequently, we designated the sample phosphated at 650 °C as single RuP_2@C. Analysis of the Brunauer-Emmett-Teller (BET) adsorption-desorption isotherm determined that the specific surface area of Ru-RuP_2@C was 260.78 $m^2 g^{-1}$. The pore size distribution of Ru-RuP_2@C predominantly appeared a mesoporous structure with an average pore size of 6.61 nm (Fig. 2c). The high specific surface area and mesoporous structure of Ru-RuP_2@C facilitated balanced electrolyte permeation and ionic diffusion, thereby expediting the reaction kinetics [30,31].

Raman spectroscopy was employed to assess the structural defects of the catalysts, where the D-band (≈ 1314 cm^{-1}) corresponds to disordered/defective C-sp^3, and G-band (≈ 1583 cm^{-1}) represents ordered graphitic C-sp^2 [32]. As shown in Fig. S4, the intensity ratio (I_D/I_G) of the HMCS support was approximately 1.46, indicating a high concentration of structural defects in the carbon support [33]. In contrast, the I_D/I_G ratio for Ru-RuP_2@C exhibited a slight decrease, likely due to the partial occupation of carbon defect sites by the Ru-RuP_2 heterojunction. The compositions and surface chemical states of Ru-RuP_2@C, RuP_2@C and Ru@C samples were examined by X-ray photoelectron spectroscopy (XPS). As showcased in Fig. S5, the XPS survey spectra displayed the characteristic peaks of C, P and Ru elements in the Ru-RuP_2@C heterostructure, correlating with the mappings results. The high-resolution Ru 3*p* XPS spectrum of Ru-RuP_2@C can be divided into two pairs of typical peaks (Fig. 2d). The peaks appeared at approximately 462.61 and 484.83 eV corresponding to the $3p_{3/2}$ and $3p_{1/2}$ orbitals of metallic Ru, respectively, while the peaks located at around 467.01 and 487.93 eV indexed to the $3p_{3/2}$ and $3p_{1/2}$ of Ru-P/O [34]. Compared to the counterparts, the binding energy of metallic Ru in Ru-RuP_2@C was higher than in RuP_2@C, but lower than in Ru@C, indicating electron interaction between RuP_2 and Ru, specifically electron transfer from interfacial RuP_2 to Ru. In the P 2*p* XPS spectra, three independent subpeaks were situated at 129.45, 132.95 and 133.90 eV, aligning with the P-Ru, P-C and P-O species, respectively (Fig. 2e) [35]. The oxidative P or Ru species in Ru-RuP_2@C probably generated by exposing to air [20,36]. Particularly, compared to single RuP_2@C, the deconvoluted peaks of Ru-P species in Ru-RuP_2@C shifted negatively, further proving the electron transfer within the Ru-RuP_2@C heterostructure. Due to the differing electronegativity of P and Ru, the formation of RuP_2 compound led to a redistribution of electrons between the atoms [37]. The stronger electron affinity of P caused it to capture some electrons from the Ru atoms, thereby reducing the electronic density of Ru [20]. As a result, in the formation of Ru-RuP_2@C catalysts, electrons tended to transfer from RuP_2 to Ru, which aligned with the XPS results mentioned earlier.

To uncover the fundamental reasons behind the enhanced HOR electrocatalytic activity of the Ru-RuP_2@C heterostructure and to delve into the interactions between RuP_2@C and Ru@C, we conducted ultraviolet photoemission spectroscopy (UPS) to analyze the interfacial charge polarization and band structure alteration [38]. As performed in Fig. 2f, the secondary electron cutoff energy of Ru-RuP_2@C (17.28 eV) was larger than those of RuP_2@C (17.12 eV) and Ru@C (16.94 eV). Concerning the vacuum energy level, the surface work functions value of Ru-RuP_2@C, RuP_2@C and Ru@C were 3.94, 4.10 and 4.28 eV, respectively. A smaller work function indicated a weaker binding ability for electrons, predisposing the electrons to disengage from the catalyst's surface [39]. For the Ru-RuP_2@C heterostructure, Ru@C exhibited a relatively strong electron-capturing capability compared to RuP_2@C, stemming from its larger work function (WF) value [40]. Consequently, it efficaciously facilitated localized charge redistribution at the heterointerface between RuP_2 and Ru, endowing the surfaces of Ru and RuP_2 with localized electrophilic and nucleophilic regions [39,41]. The energy band diagram depicted in Fig. 2g vividly elucidated the charge transfer between Ru@C and RuP_2@C. Owing to the disparity in Fermi levels, electrons spontaneously translocated from RuP_2@C to Ru@C until a Fermi equilibrium was attained, establishing a built-in electric field (BEF) and a space charge region [42]. Significantly, this BEF served as a conduit for rapid electron transit, which amplified the overall conductivity [41]. Additionally, the emergence of positively charged active centers on the RuP_2 surface catalyzed the mobilization of OH^- in alkaline electrolytes, enhancing the adsorption capacity of RuP_2@C towards OH^- and consequently facilitating the HOR process [34]. Notably, the valence electrons near the Fermi level (E_f) determine the *d*-band center (E_d) [43]. Grounded in the *d*-band center (ε_d) theory, the proximity of the *d*-band center to the E_f engenders an emptier antibonding state, enhancing the adsorption of reaction intermediates [19,44]. Compared with Ru@C and RuP_2@C, the band gap of Ru-RuP_2@C was smaller, indicating an elevational shift of the *d*-band center, which fine-tuned the active site for H intermediate adsorption.

3.2. Electrochemical HOR performance evaluation

A rotating disk electrode (RDE) system with a standard three-electrode setup in an H_2-saturated 0.1 M KOH electrolyte was used to estimate the pristine HOR electrocatalytic properties of the as-prepared catalysts. The reversible hydrogen electrode (RHE) calibration was done before electrochemical testing (Fig. S6). Optimal synthesis conditions were explored by adjusting pyrolysis temperature and metal content. Ru-RuP_2@C heterostructure with phosphating temperature at 600 °C and 3.65 % Ru content had peak HOR activity (Figs. S7-8). Subsequently, we qualitatively appraised the HOR activities of Ru-RuP_2@C, RuP_2@C, Ru@C, Pt/C and PtRu/C by comparing the current responses. As shown in Fig. 3a. Ru-RuP_2@C demonstrated the highest anodic current density spanning from kinetic to diffusion-limiting domains, whereas RuP_2@C and Ru@C showcased comparatively inferior HOR activity. This delineated that the well-defined Ru-RuP_2 interface in heterostructured electrocatalyst played a pivotal role in bolstering catalytic activity [45]. A control experiment in N_2-saturated electrolyte confirmed the anodic current was from H_2 oxidation (Fig. S9) [46]. Furthermore, we assessed the HOR polarization curves of Ru-RuP_2@C as a function of rotating rate, where the limiting current density augmented with the rotational velocity, substantiating an H_2 mass-transport controlled process (Fig. 3b) [47]. Based on the Koutecky-Levich equation, a calculated slope for Ru-RuP_2@C was 4.01 cm^2 mA^{-1} $s^{-1/2}$, closely matching the theoretical value of ~4.87 cm^2 mA^{-1} $s^{-1/2}$, supporting two-electron transfer pathway (insert in Fig. 3b) [48]. Tafel slopes (Fig. 3c) were determined to elucidate the HOR catalytic mechanism. The asymmetric nature of the Tafel plot revealed that Ru-RuP_2@C adhered to the Heyrovsky-Volmer pathway, with the Volmer step as the rate-determining step (RDS) [49].

As illustrated in Fig. 3d, the exchange current density (j_0) of samples were acquired by linear fitting of the micropolarized region (−5 to 5 mV). The j_0 of Ru-RuP_2@C was 2.73 mA cm^{-2}, showing a good intrinsic activity relative to other catalysts (Fig. 3e). The j_k value at 50 mV was computed from Koutecky-Levich equation. Ru-RuP_2@C held a geometric j_k value of 32.1 mA cm^{-2}, surpassed those of RuP_2@C (5.39 mA cm^{-2}), Ru@C (3.56 mA cm^{-2}), Pt/C (7.23 mA cm^{-2}) and PtRu/C (14.91 mA cm^{-2}). Furthermore, the j_k values were normalized by the respective mass of platinum group metals (PGM) to derive mass activity (MA) at 50 mV, offering a more precise representation of HOR activity (Fig. 3f). Ru-RuP_2@C showcased a MA of 2.87 mA μg_{Ru}^{-1}, signally higher than other synthesized catalysts and recently reported catalysts. Stability, a crucial metric for assessing the holistic performance of catalysts, was appraised through accelerated degradation testing (ADT) and chronoamperometry [12]. The ADT was performed by cycling the catalyst between 0 V and 1.0 V (vs. RHE) at a scan rate of 100 mV s^{-1} in H_2-saturated 0.1 M KOH. After 1000 cycles of cyclic voltammetry (CV), the polarization curves of Ru-RuP_2@C coincided well (Fig. 3g). Whereas the activity of commercial Pt/C and commercial PtRu/C manifested a noticeable decrease under the same conditions. Moreover,

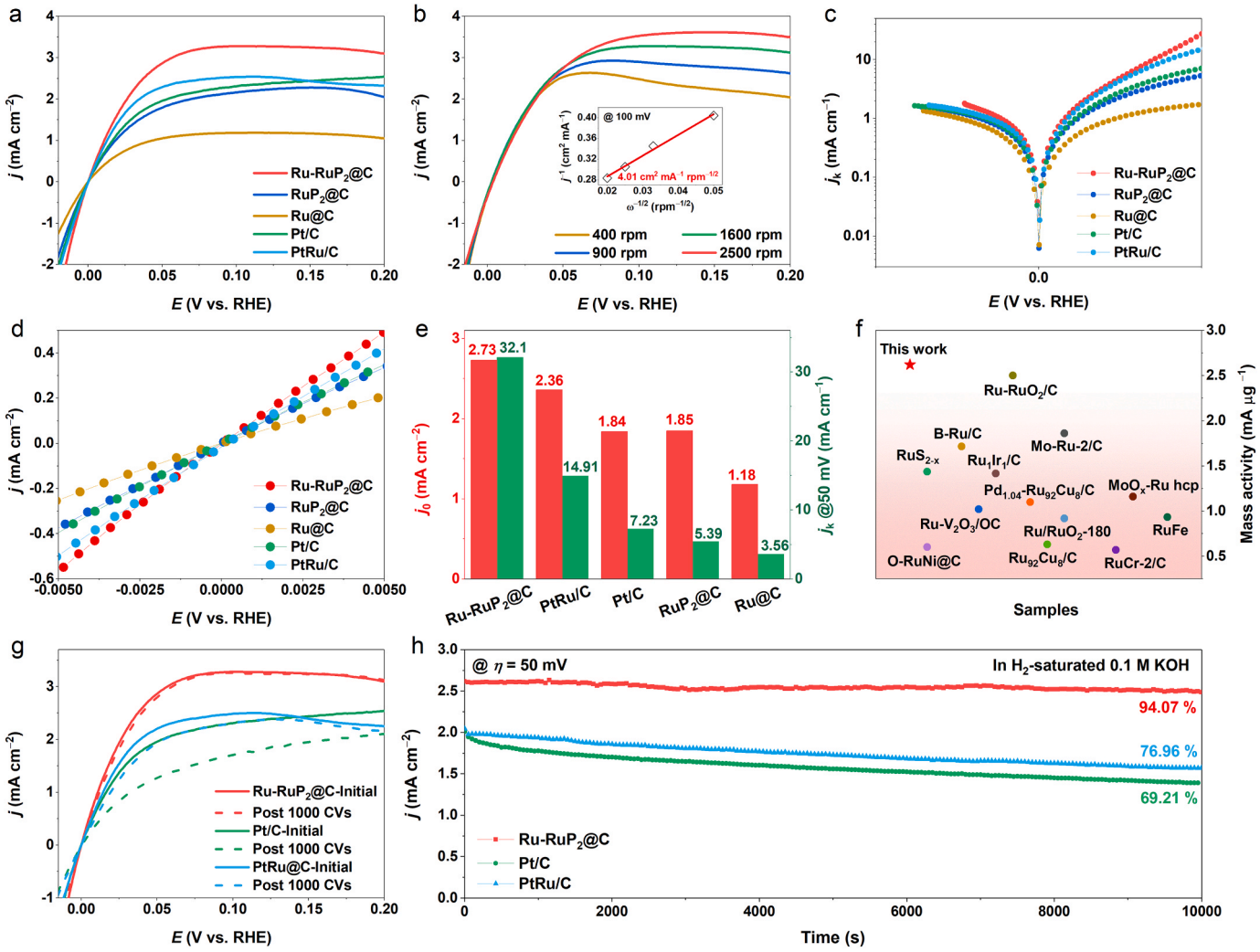

Fig. 3. (a) HOR polarization curves of Ru-RuP_2@C, RuP_2@C, Ru@C, Pt/C and PtRu/C. (b) Polarization curves of Ru-RuP_2@C at various rotation speeds, inset depicts corresponding Koutecky−Levich plot. (c) Tafel plots. (d) Linear fitting curves in −5~5 mV region. (e) Comparison of j_k and j_0 for studied electrocatalysts. (f) Compared the MA with other recently reported alkaline HOR catalysts. (g) HOR polarization curves before and after 1000 cycles and (h) chronoamperometry (*j*-*t*) responses were recorded on Ru-RuP_2@C, Pt/C and PtRu/C.

chronoamperometric (*j*-t) assessments (Fig. 3h) were implemented on the RDE to appraise the sustained HOR catalytic ability of Ru-RuP_2@C at 50 mV. The current density maintained HOR reactivity without significant deviation throughout the test, while the Pt/C and PtRu/C catalysts exhibited an evident decline in activity after 10000 s. These results collectively corroborated the outstanding long-term stability of Ru-RuP_2@C for HOR. After the ADT testing, Ru-RuP_2@C powder was collected and physically characterized. As exhibited in Fig. S10, XRD patterns confirmed that the crystalline structure of Ru-RuP_2@C was well-preserved. Additionally, we observed that Ru-RuP_2@C retained both Ru and Ru-P signals, although the oxidation state of Ru increased, which aligned with theoretical predictions due to the long-term H_2 oxidation process (Fig. S11).

For utilization in alkaline fuel cells, an exceptional HOR catalyst must possesses high CO resistance. This necessity arises because crude hydrogen typically contains trace concentration of CO, which can swiftly poison the catalysts [50,51]. Hence, the anti-CO poisoning ability of Ru-RuP_2@C and other reference samples were evaluated by measuring HOR polarization curves in both pure H_2-saturated and H_2/1000 ppm CO-saturated 0.1 M KOH electrolyte. Compared to the test data in pure H_2-saturated media (dashed line), the HOR current density of Ru-RuP_2@C (Fig. 4a) at 50 mV potential only decreased by 4.06 % under the synergistic electron interaction generated by the heterogeneous interface. This further indicated that the formation of the heterogeneous interface of Ru-RuP_2 helped to improve the catalyst's resistance to CO poisoning. In contrast, commercial PtRu/C, Pt/C and other comparative samples were sharply poisoned in the same environment. Specifically, the HOR current density of RuP_2@C, Ru@C, commercial PtRu/C and commercial Pt/C in H_2/1000 ppm CO exhibited current reductions of 34.09 %, 66.89 %, 19.91 % and 84.03 %, respectively (Figs. 4b-e).

To further scrutinize the time-dependent CO tolerance performance of the samples, examinations were conducted at a consistent overpotential of 50 mV to acquire the chronoamperometry response curves (Fig. 4 f). Following a stability test of 1000 s, the relative current density of Ru-RuP_2@C remained at 84.05 %, greatly surpassing those of RuP_2@C, Ru@C, commercial PtRu/C and commercial Pt/C. This reaffirmed that the electron interactions induced by the built-in electric field at the heterointerface due to the difference in the work function, was favorable to the catalyst's resistance to CO poisoning. Furthermore, to elucidate the reasons behind the disparities in anti-CO poisoning capacity among the synthesized catalysts, we conducted CO stripping experiments in 0.1 M KOH solution (Fig. 4 g). The CO stripping peak potential of Ru-RuP_2@C was negatively shifted, with a peak situated at 0.69 V compared to RuP_2@C (0.76 eV) and Ru@C (0.77 V), suggesting that CO adsorption on Ru sites was weaker in Ru-RuP_2@C, thus leaving

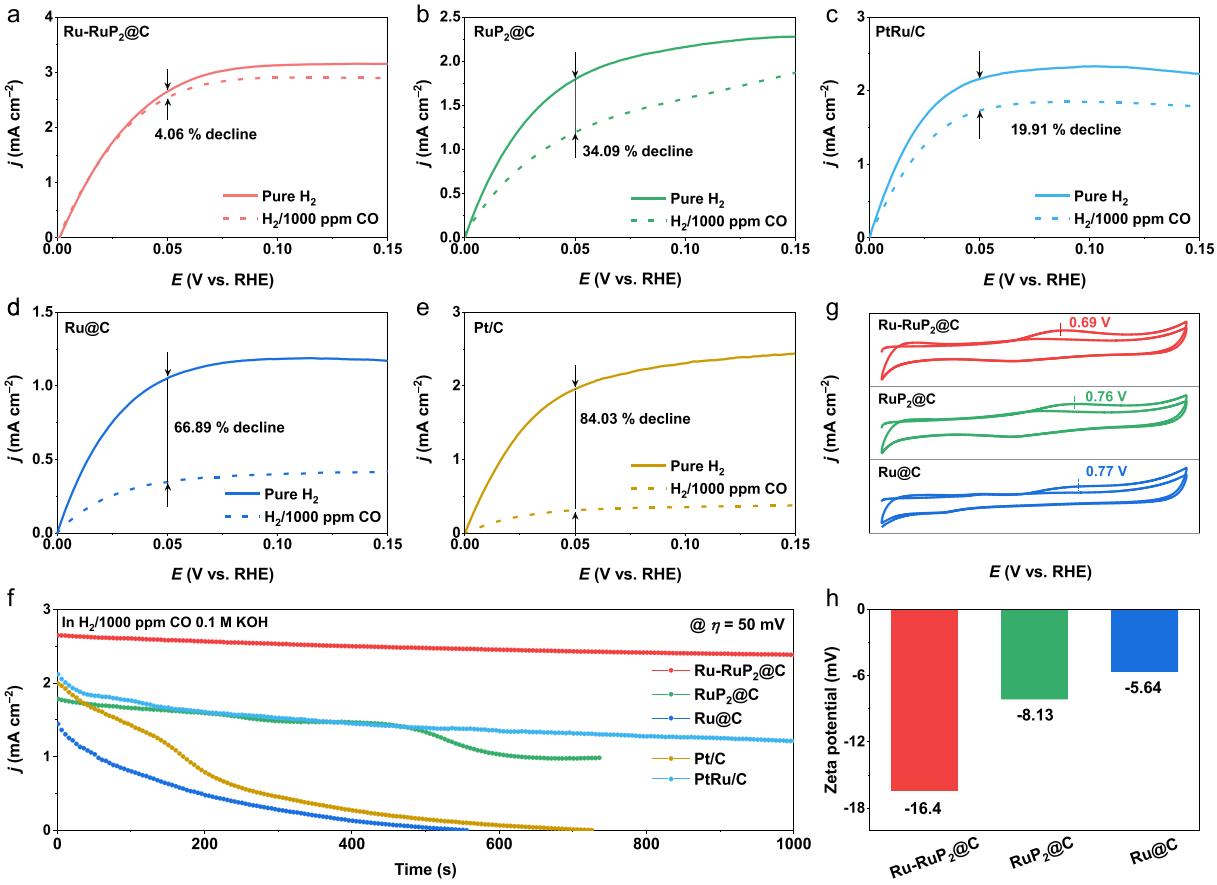

Fig. 4. (a-e) HOR performance of the Ru-RuP$_2$@C, RuP$_2$@C, PtRu/C, Ru@C, and Pt/C in pure H_2 and H_2/1000 ppm CO. (f) Chronoamperometry (*j*–t) response at 50 mV in H_2/1000 ppm CO-saturated 0.1 M KOH. (g) CO stripping curves and (h) zeta potentials of Ru-RuP$_2$@C, RuP$_2$@C and Ru@C.

more active Ru sites for the adsorption and oxidation of H_2 and displaying high HOR activity in the existence of CO [52,53]. Beyond that, zeta potential characterization was performed to measure the OH adsorption capacity and compare the samples' OHBE values. As demonstrated in Fig. 4 h and Fig. S12, the average potential value of Ru-RuP$_2$@C (-16.4 mV) was obviously lower than those of RuP$_2$@C (-8.13 mV) and Ru@C (-5.64 mV), certifying the stronger OH adsorption on Ru-RuP$_2$@C. Consequently, the enhanced OHBE allowed Ru-RuP$_2$@C to manifest accelerated kinetic characteristics in alkaline HOR.

3.3. Theoretical study

To gain an in-depth comprehension of the catalytic source of Ru-RuP$_2$@C in facilitating the HOR, theoretical simulations utilizing density functional theory (DFT) calculations were undertaken. A set of catalyst model systems for Ru (001), RuP$_2$ (020), and Ru-RuP$_2$ heterostructure were appropriately constructed (Fig. S13). The local charge density analysis of Ru-RuP$_2$@C in Fig. 5a revealed that there was evident charge accumulation in Ru within the Ru-RuP$_2$ heterostructure, especially in the interfacial Ru atoms in the Ru domains. This behavior was closely associated with the strong interactions at the heterointerface, accompanied by the electrons transfer from RuP$_2$ to Ru, which corresponded to the XPS and UPS results. Compared to Ru@C and RuP$_2$@C, the Ru-RuP$_2$@C electrocatalyst exhibited a higher total density of states (DOS) occupancy near the Fermi level. This suggested that the interfacial electronic coupling between Ru and RuP$_2$ reduced the charge transfer resistance (Fig. 5b) [54]. It also indicated that there were more electronic states available for electron occupation and mobility at this energy level, leading to enhanced electronic conductivity [55]. In Fig. 5c, the *d*-band center of Ru-RuP$_2$@C, RuP$_2$@C and Ru@C were determined to be −1.74, −2.11 and −2.70 eV, respectively, indicating the Ru-RuP$_2$@C shifted up closer to Fermi level than those of RuP$_2$@C and Ru@C. Generally speaking, the *d*-band center is correlates with reaction intermediates' binding affinity [42]. An upward displacement of the *d*-band center for Ru-RuP$_2$@C signified an augmentation in the adhesive force between the catalyst and intermediates, which was advantageous for lowing potential energy barriers, thereby amplifying the HOR catalytic efficacy.

It is extensively recognized that hydrogen binding energy (HBE) and hydroxyl binding energy (OHBE) are two fundamental descriptors for HOR performance [56]. In light of this, the adsorption behavior of H_{ad} and OH_{ad} on the Ru-RuP$_2$@C heterostructure was simulated, along with catalysts of pure RuP$_2$@C and Ru@C surfaces as comparative subjects (Figs. S14-15). As illuminated in Fig. 5d, the Ru-RuP$_2$@C showcased an attenuated HBE with a value of −0.12 eV, which was closer to the ideal zero Gibbs free energy than those of pure RuP$_2$@C (-0.22 eV) and Ru@C (-0.43 eV), implying a favorable HOR process. Similarly, the OHBE for the Ru-RuP$_2$@C heterostructure, RuP$_2$@C and Ru@C were calculated to be −0.26, −0.07 and 0.31 eV, respectively (Fig. 5e), confirming that the Ru-RuP$_2$@C possessed stronger OH adsorption, which was beneficial for facilitating the removal of adsorbed CO and enhancing the anti-CO poisoning ability [57]. Compared with RuP$_2$@C (-1.48 eV) and Ru@C (-1.59 eV), the adsorption of CO on Ru-RuP$_2$@C (-0.41 eV) was significantly weakened (Fig. 5f and Fig. S16). This result elucidated the superior CO-tolerance ability of Ru-RuP$_2$@C, which aligned with the comparison of desorption peaks of CO for Ru-RuP$_2$@C and other samples.

Subsequently, the free energy profiles for the alkaline HOR process on the Ru-RuP$_2$@C heterostructure, RuP$_2$@C and Ru@C models were determined (Fig. 5g). The first step, involving the adsorption of OH or H,

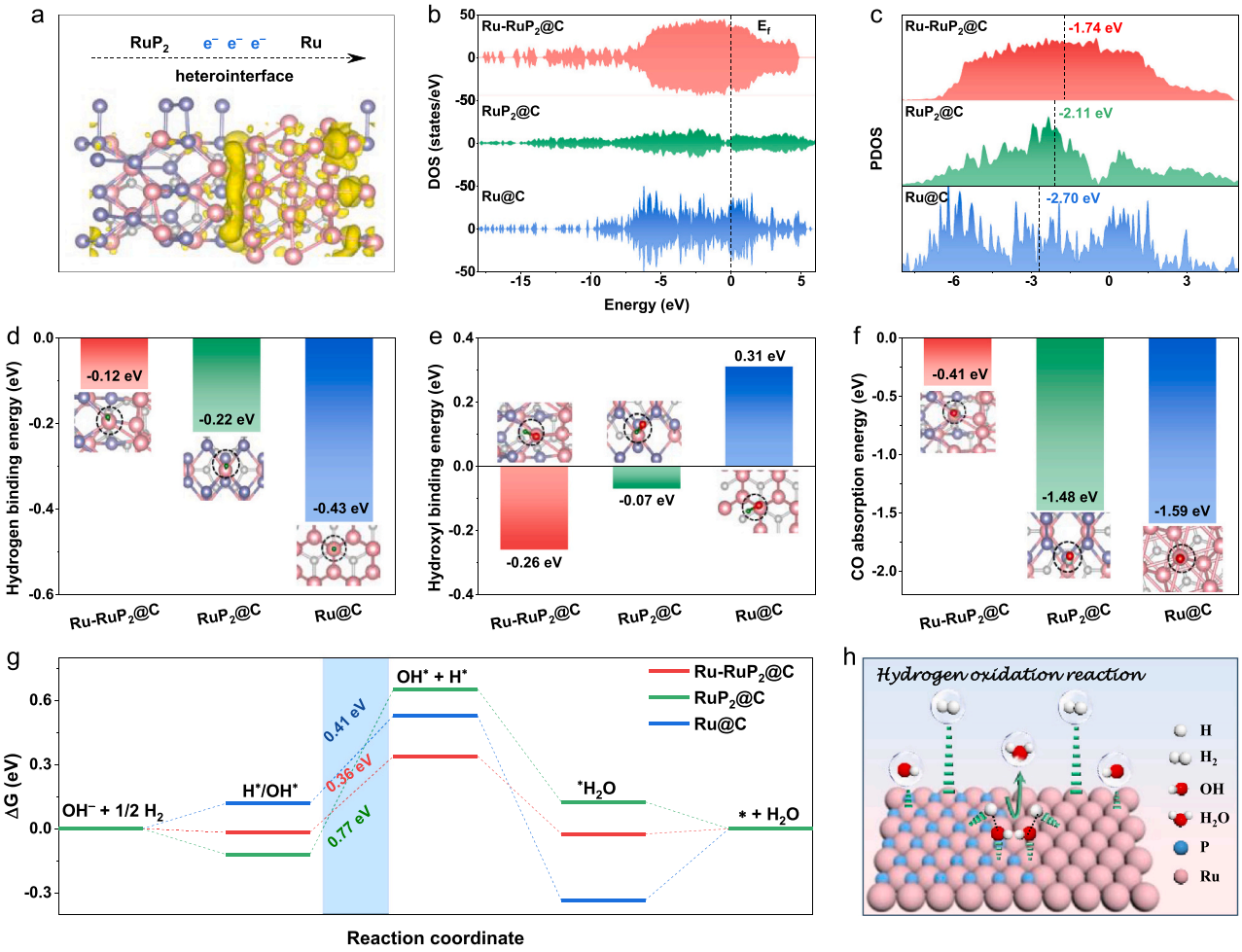

Fig. 5. (a) Local charge density of the Ru-RuP_2@C model. The pink and purple balls represent Ru and P atoms, respectively. (b) The density of state (DOS) plots. (c) The PDOS and *d*-band center value of Ru in Ru-RuP_2@C, RuP_2@C and Ru@C. (d-f) Calculated HBEs, OHBEs, and CO absorption energies on Ru-RuP_2@C, RuP_2@C and Ru@C models. (g) Gibbs free energy profiles of basic HOR on the surfaces of Ru-RuP_2@C, RuP_2@C and Ru@C. (h) Schematic illustration of the basic HOR mechanism on Ru-RuP_2@C.

was spontaneous for Ru-RuP_2@C and RuP_2@C, whereas it was endothermic for Ru@C. For Ru-RuP_2@C, the H*+OH* (0.36 eV) and water-desorption (0.02 eV) steps were both endothermic, consistent with RuP_2@C (0.77 and 0.13 eV, respectively). Ru@C was endothermic only for the H*+OH* (0.41 eV) step, suggesting that the potential-determining step (PDS) was the H*+OH* step for all three catalysts. Signally, the energy barrier in H*+OH* step for Ru-RuP_2@C was lower than those of RuP_2@C and Ru@C, emphasizing the importance of constructing controllable Ru-RuP_2 heterogeneous structures. Theoretical simulation results indicated that Ru-RuP_2@C heterostructure yielded optimal HBE and OHBE that bolstered the HOR energetics. Fig. 5h depicted a vivid and intuitive bifunctional mechanism of HOR catalysis on the Ru-RuP_2@C model to offer more insight into the reaction process.

3.4. Performance of AEMFCs

Encouraged by the superior HOR activity, CO tolerance, and stability of the Ru-RuP_2@C electrocatalyst, we employed it as the anode catalyst for AEMFC. Membrane electrode assemblies (MEAs) were fabricated using Ru-RuP_2@C as the anode (0.2 mg_{Ru} cm^{-2}) and commercial Pt/C as the cathode (0.4 mg_{Pt} cm^{-2}). As shown in Figs. 6a-b, the peak power density (PPD) of the Ru-RuP_2@C anode reached 521 mW cm^{-2} under H_2-O_2 operating conditions, closely matching the performance of the Pt/C (534 mW cm^{-2}). Notably, the performance difference between Ru-RuP_2@C and Pt/C in the low-polarization region was minimal. Although the PPD of the Ru-RuP_2@C anode was slightly lower than that of Pt/C, their current densities at the typical operating potential for automotive applications (around 0.65 V) were comparable (Fig. 6c), indicating strong potential for practical applications [6]. Furthermore, as illustrated in Fig. 6d and Table S4, the PPD value of Ru-RuP_2@C outperformed many existing noble and non-noble metal-based catalysts.

4. Conclusion

In conclusion, we have engineered a distinctive Ru-RuP_2@C electrocatalyst with affluent heterointerfaces through a controllable phosphating strategy. The hollow mesopore spherical structure of the Ru-RuP_2@C offered an abundance of active sites and quickened ion/mass transport. Notably, the redistribution of interfacial electrons optimized the bonding strength between Ru and the intermediate and shifted HOR activity toward the apex of the volcanic curve. As expected, the Ru-RuP_2@C demonstrated a higher mass activity and exchange current density, exceeding those of single-component materials and benchmark Pt/C. To its credit, Ru-RuP_2@C possessed robust CO resistance, with only a 4.06 % decrease in current density in saturated-H_2/1000 ppm CO. When further employed as an anode catalyst for AEMFC, Ru-RuP_2@C achieved a peak power density of 521 mW cm^{-2}, approaching the performance of state-of-the-art Pt catalysts and surpassing most documented anode catalysts. Spectroscopic characterization and theoretical simulations revealed the imperative role of the asymmetric charge

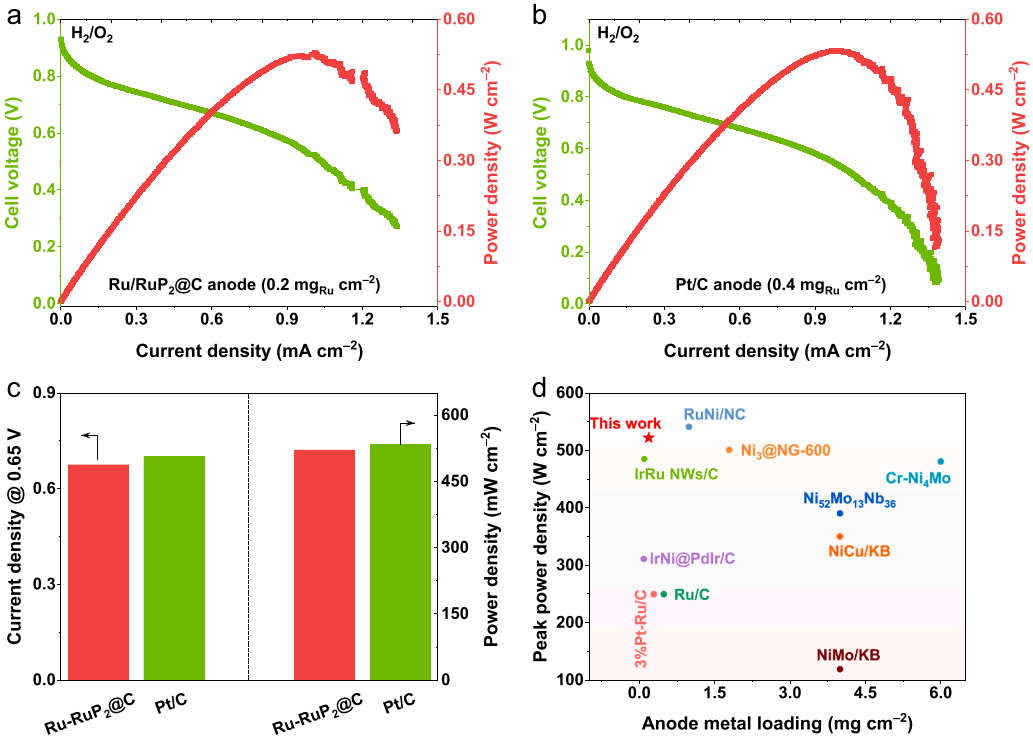

Fig. 6. Polarization and power density curve of H_2/O_2 AEMFC for (a) Ru-RuP_2@C and (b) Pt/C catalysts. (c) Comparison of the PPD and the current density at 0.65 V of the catalysts. (d) Comparison of peak power density of AEMFCs reported recently.

distributions, stemming from the disparity in work function at the Ru-RuP_2 interface, which generated a strong interfacial BEF. This BEF effect facilitated OH adsorption on the positive charge-enriched RuP_2 side, while optimizing H adsorption on the negatively charged Ru side. This discovery underscores the potential of manipulating interfacial BEF to modulate surface charge distribution, presenting a promising avenue for developing advanced catalysts in diverse electrocatalytic applications.

CRediT authorship contribution statement

Yi Liu: Conceptualization, Writing – original draft. **Lianrui Cheng**: Methodology. **Shuqing Zhou**: Investigation. **Chenggong Niu**: Data curation. **Tayirjan Taylor Isimjan**: Writing – review & editing. **Xiulin Yang**: Writing – review & editing, Supervision, Funding acquisition.

Declaration of Competing Interest

The authors declare that they have no known competing financial interests or personal relationships that could have appeared to influence the work reported in this paper. The authors declare no conflict of interest.

Acknowledgements

This work has been supported by the National Natural Science Foundation of China (no. 52363028, 21965005), Natural Science Foundation of Guangxi Province (2021GXNSFAA076001, 2018GXNSFAA294077), Guangxi Technology Base and Talent Subject (GUIKE AD23023004, GUIKE AD20297039). Innovation Project of Guangxi Graduate Education (YCSW2024228).

Appendix A. Supporting information

Supplementary data associated with this article can be found in the online version at doi:10.1016/j.apcatb.2024.124709.

Data availability

Data will be made available on request.

References

[1] C. Yang, F. Yue, G. Wang, W. Luo, Activating and identifying the active site of RuS_2 for alkaline hydrogen oxidation electrocatalysis, Angew. Chem. Int. Ed. 63 (2024) e202401453.
[2] D. Guan, J. Zhou, Y.-C. Huang, C.-L. Dong, J.-Q. Wang, W. Zhou, Z. Shao, Screening highly active perovskites for hydrogen-evolving reaction via unifying ionic electronegativity descriptor, Nat. Commun. 10 (2019) 3755.
[3] Y.-H. Wang, Y. Yang, F.-Y. Gao, X.-L. Zhang, L. Zhu, H.-K. Yan, P.-P. Yang, M.-R. Gao, Unraveling stoichiometry effect in nickel-tungsten alloys for efficient hydrogen oxidation catalysis in alkaline electrolytes, Angew. Chem. Int. Ed. 63 (2024) e202407613.
[4] H. Shi, Y. Yang, P. Meng, J. Yang, W. Zheng, P. Wang, Y. Zhang, X. Chen, Z. Cheng, C. Zong, D. Wang, Q. Chen, Local charge transfer unveils antideactivation of Ru at high potentials for the alkaline hydrogen oxidation reaction, J. Am. Chem. Soc. 146 (2024) 16619–16629.
[5] G. Shi, T. Tano, D.A. Tryk, A. Iiyama, M. Uchida, K. Kakinuma, Pt nanorods supported on Nb-doped ceria: A promising anode catalyst for polymer electrolyte fuel cells, Electrochem. Commun. 163 (2024) 107733.
[6] J. Fang, H. Wang, Q. Dang, H. Wang, X. Wang, J. Pei, Z. Xu, C. Chen, W. Zhu, H. Li, Y. Yan, Z. Zhuang, Atomically dispersed Iridium on Mo_2C as an efficient and stable alkaline hydrogen oxidation reaction catalyst, Nat. Commun. 15 (2024) 4236.
[7] X. Mu, S. Liu, M. Zhang, Z. Zhuang, D. Chen, Y. Liao, H. Zhao, S. Mu, D. Wang, Z. Dai, Symmetry-Broken Ru Nanoparticles with Parasitic Ru-Co Dual-Single Atoms Overcome the Volmer Step of Alkaline Hydrogen Oxidation, Angew. Chem. Int. Ed. 63 (2024) e202319618.
[8] Y. Zhou, C. Tao, J. Ke, X. Dai, J. Guo, L. Zhang, T. Li, C. Yan, T. Qian, Balancing the Binding of Intermediates Enhances Alkaline Hydrogen Oxidation on D-Band Center Modulated Pd Sites, Inorg. Chem. (2024).
[9] R. Nandan, H. Nara, H.N. Nam, Q.M. Phung, Q.P. Ngo, J. Na, J. Henzie, Y. Yamauchi, Tailored design of mesoporous nanospheres with high entropic alloy sites for efficient redox electrocatalysis, Adv. Sci. (2024) 2402518.
[10] Y. Qiu, L. Xin, Y. Li, I.T. McCrum, F. Guo, T. Ma, Y. Ren, Q. Liu, L. Zhou, S. Gu, M. J. Janik, W. Li, BCC-phased PdCu alloy as a highly active electrocatalyst for hydrogen oxidation in alkaline electrolytes, J. Am. Chem. Soc. 140 (2018) 16580–16588.
[11] J.-T. Ren, Y.-S. Wang, Y.-J. Song, L. Chen, Z.-Y. Yuan, Interface engineering of in−situ formed nickel hydr(oxy)oxides on nickel nitrides to boost alkaline hydrogen electrocatalysis, Appl. Catal. B: Environ. 309 (2022) 121279.
[12] Z. Cui, Z. Ren, C. Ma, B. Chen, G. Chen, R. Lu, W. Zhu, T. Gan, Z. Wang, Z. Zhuang, Y. Han, Dilute RuCo Alloy Synergizing Single Ru and Co Atoms as Efficient and CO-

Resistant Anode Catalyst for Anion Exchange Membrane Fuel Cells, Angew. Chem. Int. Ed. 63 (2024) e202404761.
[13] J. Park, H. Kim, S. Kim, S.Y. Yi, H. Min, D. Choi, S. Lee, J. Kim, J. Lee, Boosting Alkaline Hydrogen Oxidation Activity of Ru Single-Atom Through Promoting Hydroxyl Adsorption on Ru/WC_{1-x} Interfaces, Adv. Mater. 36 (2023) 2308899.
[14] P. Han, X. Yang, L. Wu, H. Jia, J. Chen, W. Shi, G. Cheng, W. Luo, A. Highly-Efficient Boron Interstitially, Inserted Ru Anode Catalyst for Anion Exchange Membrane Fuel Cells, Adv. Mater. 36 (2023) 2304496.
[15] Y. Zhao, X. Zhang, Y. Gao, Z. Chen, Z. Li, T. Ma, Z. Wu, L. Wang, S. Feng, Heterostructure of RuO_2-RuP_2/Ru Derived from HMT-based Coordination Polymers as Superior pH-Universal Electrocatalyst for Hydrogen Evolution Reaction, Small 18 (2022) 2105168.
[16] L. Chen, H.Y. Wang, W.W. Tian, L. Wang, M.L. Sun, J.T. Ren, Z.Y. Yuan, Enabling internal electric field in heterogeneous nanosheets to significantly accelerate alkaline hydrogen electrocatalysis, Small 19 (2023) 2307252.
[17] W. Zhang, L. Yang, Z. Li, G. Nie, X. Cao, Z. Fang, X. Wang, S. Ramakrishna, Y. Long, L. Jiao, Regulating Hydrogen/Oxygen Species Adsorption via Built-in Electric Field -Driven Electron Transfer Behavior at the Heterointerface for Efficient Water Splitting, Angew. Chem. Int. Ed. 63 (2024) e202400888.
[18] Y. Cong, D. Dou, L. Zhang, H. Wang, M. Liu, L. Chen, Q. Zhao, C. Li, Synergistic interactions of electronic modulation and low crystallization in Ru-RuO_2/C heterostructure for highly efficient multifunctional electrocatalysis, Fuel 367 (2024) 131472.
[19] S. Zhang, C. Tan, R. Yan, X. Zou, F.-L. Hu, Y. Mi, C. Yan, S. Zhao, Constructing built-in electric field in heterogeneous nanowire arrays for efficient overall water electrolysis, Angew. Chem. Int. Ed. 62 (2023) e202302795.
[20] H. Du, Z. Du, T. Wang, B. Li, S. He, K. Wang, L. Xie, W. Ai, W. Huang, Unlocking interfacial electron transfer of ruthenium phosphides by homologous core-shell design toward efficient hydrogen evolution and oxidation, Adv. Mater. 34 (2022) 2204624.
[21] Y. Jin, X. Fan, W. Cheng, Y. Zhou, L. Xiao, W. Luo, The role of phosphorus on alkaline hydrogen oxidation electrocatalysis for ruthenium phosphides, Angew. Chem. Int. Ed. N./a (2024) e202406888.
[22] Y. Liu, L. Cheng, S. Zhou, Y. Yang, C. Niu, T.Taylor Isimjan, B. Wang, X. Yang, Revealing interfacial charge redistribution of homologous Ru-RuS_2 heterostructure toward robust hydrogen oxidation reaction, J. Energy Chem. 94 (2024) 332–339.
[23] M. Guo, Z. Huang, Y. Qu, L. Wang, H. Li, T.T. Isimjan, X. Yang, Synergistic effect and nanostructure engineering of three-dimensionally hollow mesoporous spherical Cu_3P/TiO_2 in aqueous/flexible Zn–air batteries, Appl. Catal. B Environ. 320 (2023) 121991.
[24] D. Zhao, K. Sun, W.C. Cheong, L. Zheng, C. Zhang, S. Liu, X. Cao, K. Wu, Y. Pan, Z. Zhuang, B. Hu, D. Wang, Q. Peng, C. Chen, Y. Li, Synergistically Interactive Pyridinic-N-MoP Sites: Identified Active Centers for Enhanced Hydrogen Evolution in Alkaline Solution, Angew. Chem. Int. Ed. 59 (2020) 8982–8990.
[25] Y. Xu, C. Du, Q. Shen, J. Huang, X. Zhang, J. Chen, Well-dispersed pyrite-type RuS_2 nanocrystals anchored on porous nitrogen and sulfur co-doped hollow carbon spheres for enhanced alkaline hydrogen evolution, Chem. Eng. J. 417 (2021) 129318.
[26] S. Gong, W. Wang, C. Zhang, M. Zhu, R. Lu, J. Ye, H. Yang, C. Wu, J. Liu, D. Rao, S. Shao, X. Lv, Tuning the Metal Electronic Structure of Anchored Cobalt Phthalocyanine via Dual-Regulator for Efficient CO_2 Electroreduction and Zn–CO_2 Batteries, Adv. Funct. Mater. 32 (2022) 2110649.
[27] M. Guo, L. Wang, Z. Huang, H. Li, T.T. Isimjan, X. Yang, Modulating the Energy Barrier via the Synergism of Cu_3P and CoP to Accelerate Kinetics for Bolstering Oxygen Electrocatalysis in Zn-Air Batteries, ACS Nano 18 (2024) 17901–17912.
[28] L. Wei, W. Yan, Z. Huang, R. Li, Q. Kong, W.-H. Huang, C.-W. Pao, Z. Hu, H. Lin, N. Chen, Y. Xu, H. Geng, X. Huang, Phase and Interface Engineering of a Ru-Sn Nanocatalyst for Enhanced Alkaline Hydrogen Oxidation Reaction, Energy Environ. Sci. (2024).
[29] R. Ge, S. Wang, J. Su, Y. Dong, Y. Lin, Q. Zhang, L. Chen, Phase-selective synthesis of self-supported RuP films for efficient hydrogen evolution electrocatalysis in alkaline media, Nanoscale 10 (2018) 13930–13935.
[30] V. Jose, H. Hu, E. Edison, W. Manalastas, Jr, H. Ren, P. Kidkhunthod, S. Sreejith, A. Jayakumar, J.M.V. Nsanzimana, M. Srinivasan, J. Choi, J.M. Lee, Modulation of Single Atomic Co and Fe Sites on Hollow Carbon Nanospheres as Oxygen Electrodes for Rechargeable Zn-Air Batteries, Small Methods 5 (2021) e2000751.
[31] L. Peng, C.T. Hung, S. Wang, X. Zhang, X. Zhu, Z. Zhao, C. Wang, Y. Tang, W. Li, D. Zhao, Versatile Nanoemulsion Assembly Approach to Synthesize Functional Mesoporous Carbon Nanospheres with Tunable Pore Sizes and Architectures, J. Am. Chem. Soc. 141 (2019) 7073–7080.
[32] A. Gupta, S.R. Dhakate, P. Pal, A. Dey, P.K. Iyer, D.K. Singh, Effect of graphitization temperature on structure and electrical conductivity of poly-acrylonitrile based carbon fibers, Diam. Relat. Mater. 78 (2017) 31–38.
[33] J. Wu, Y. Zhou, H. Nie, K. Wei, H. Huang, F. Liao, Y. Liu, M. Shao, Z. Kang, Carbon dots regulate the interface electron transfer and catalytic kinetics of Pt-based alloys catalyst for highly efficient hydrogen oxidation, J. Energy Chem. 66 (2022) 61–67.
[34] L. Su, Y. Jin, D. Gong, X. Ge, W. Zhang, X. Fan, W. Luo, The Role of Discrepant Reactive Intermediates on Ru-Ru_2P Heterostructure for pH-Universal Hydrogen Oxidation Reaction, Angew. Chem. Int. Ed. 62 (2022) e202215585.
[35] Y. Jiang, L. Du, W. Sun, Q. Zhang, Y. Su, M. Sun, G. Yin, Constructing tungsten doping RuP_2@Carbon dots for enhanced hydrogen evolution reaction in acidic and alkaline media, Int. J. Hydrog. Energy 51 (2023) 725–732.
[36] Q. Chang, J. Ma, Y. Zhu, Z. Li, D. Xu, X. Duan, W. Peng, Y. Li, G. Zhang, F. Zhang, X. Fan, Controllable Synthesis of Ruthenium Phosphides (RuP and RuP_2) for pH-Universal Hydrogen Evolution Reaction, ACS Sustain. Chem. Eng. 6 (2018) 6388–6394.
[37] M. Cheng, H. Geng, Y. Yang, Y. Zhang, C.C. Li, Optimization of the Hydrogen-Adsorption Free Energy of Ru-Based Catalysts towards High-Efficiency Hydrogen Evolution Reaction at all pH, Chem. Eur. J. 25 (2019) 8579–8584.
[38] Y. Li, C. Yang, J. Yue, H. Cong, W. Luo, Polymorphism-Interface-Induced Work Function Regulating on Ru Nanocatalyst for Enhanced Alkaline Hydrogen Oxidation Reaction, Adv. Funct. Mater. 33 (2023) 2211586.
[39] H. Ding, Z. Zhao, H. Zeng, X. Li, K. Cui, Y. Zhang, X. Chang, Heterojunction-Induced Local Charge Redistribution Boosting Energy-Saving Hydrogen Production via Urea Electrolysis, ACS Mater. Lett. 6 (2024) 1029–1041.
[40] C. Feng, W. Zhou, H. Wu, Q. Huo, J. Shao, X. Li, H. Yang, Q. Hu, C. He, Tuning work function difference of copper/cobalt oxides heterointerfaces enables efficient electrochemical nitrate reduction, Appl. Catal. B Environ. 341 (2023) 123280.
[41] C. Wang, H. Lu, Z. Mao, C. Yan, G. Shen, X. Wang, Bimetal Schottky Heterojunction Boosting Energy-Saving Hydrogen Production from Alkaline Water via Urea Electrocatalysis, Adv. Funct. Mater. 30 (2020) 2000556.
[42] J. Sun, H. Xue, J. Sun, N. Guo, T. Song, Y.-R. Hao, Q. Wang, Interfacial charge redistribution to promote the catalytic activity of Vs-CoP-CoS_2/C n-n heterojunction for oxygen evolution, Chin. Chem. Lett. 35 (2024) 109002.
[43] Z. Huang, M. Liao, S. Zhang, L. Wang, M. Gao, Z. Luo, T.T. Isimjan, B. Wang, X. Yang, Valence electronic engineering of superhydrophilic Dy-evoked Ni-MOF outperforming RuO_2 for highly efficient electrocatalytic oxygen evolution, J. Energy Chem. 90 (2024) 244–252.
[44] L. Wang, X. Hu, H. Li, Z. Huang, J. Huang, T.T. Isimjan, X. Yang, Engineering built-in electric fields in oxygen-deficient MnO-CeO_2@Cs catalysts: enhanced performance and kinetics for the oxygen reduction reaction in aqueous/flexible zinc–air batteries, Green. Chem. 26 (2024) 2011–2020.
[45] X. Zhang, L. Xia, G. Zhao, B. Zhang, Y. Chen, J. Chen, M. Gao, Y. Jiang, Y. Liu, H. Pan, W. Sun, Fast and durable alkaline hydrogen oxidation reaction at the electron-deficient ruthenium–ruthenium oxide interface, Adv. Mater. 35 (2023) 2208821.
[46] Y. Yang, L. Shi, Q. Liang, Y. Liu, J. Dong, T.T. Isimjan, B. Wang, X. Yang, Uleashing efficient and CO-resilient alkaline hydrogen oxidation of Pd_3P through phosphorus vacancy defect engineering, Chin. J. Catal. 56 (2024) 176–187.
[47] R. Samanta, B.K. Manna, R. Trivedi, B. Chakraborty, S. Barman, Hydrogen spillover enhances alkaline hydrogen electrocatalysis on interface-rich metallic Pt-supported MoO_3, Chem. Sci. 15 (2024) 364–378.
[48] K.-R. Yeo, K. Ji Choi, S.-K. Kim, Enhanced alkaline hydrogen oxidation reaction using electrodeposited Ni-Ir alloy catalysts, Appl. Surf. Sci. 614 (2023) 156207.
[49] X. Tian, P. Zhao, W. Sheng, Hydrogen Evolution and Oxidation: Mechanistic Studies and Material Advances, Adv. Mater. 31 (2019) 1808066.
[50] J. Cai, X. Zhang, Z. Lyu, H. Huang, S. Wang, L. Fu, Q. Wang, X.-F. Yu, Z. Xie, S. Xie, Host–Guest Ensemble Effect on Dual-Pt atom-on-Rh Nanosheets Enables High-Efficiency and Anti-CO Alkaline Hydrogen Oxidation, ACS Catal. 13 (2023) 6974–6982.
[51] P. Wang, Y. Yang, W. Zheng, Z. Cheng, C. Wang, S. Chen, D. Wang, J. Yang, H. Shi, P. Meng, P. Wang, H. Tong, J. Chen, Q. Chen, V–O Species-Doped Carbon Frameworks Loaded with Ru Nanoparticles as Highly Efficient and CO-Tolerant Catalysts for Alkaline Hydrogen Oxidation, J. Am. Chem. Soc. 145 (2023) 27867–27876.
[52] C. Zhan, Y. Xu, L. Bu, H. Zhu, Y. Feng, T. Yang, Y. Zhang, Z. Yang, B. Huang, Q. Shao, X. Huang, Subnanometer high-entropy alloy nanowires enable remarkable hydrogen oxidation catalysis, Nat. Commun. 12 (2021) 6261.
[53] C.A. Campos-Roldán, R. Chattot, F. Pailloux, A. Zitolo, J. Rozière, D.J. Jones, S. Cavaliere, Lanthanide contraction effect on the alkaline hydrogen evolution and oxidation reactions activity in platinum–rare earth nanoalloys, J. Mater. Chem. A 12 (2024) 1253–1258.
[54] L. Wang, Z. Xu, C. Kuo, J. Peng, F. Hu, L. Li, H. Chen, J. Wang, S. Peng, Stabilizing Low-Valence Single Atoms by Constructing Metalloid Tungsten Carbide Supports for Efficient Hydrogen Oxidation and Evolution, Angew. Chem. Int. Ed. 62 (2023) e202311937.
[55] J. Guo, J. Liu, X. Zhang, X. Guan, M. Zeng, J. Shen, J. Zou, Q. Chen, T. Wang, D. Qian, Synergistically coupling Pt with Ni towards accelerated water dissociation for enhanced alkaline hydrogen evolution, J. Mater. Chem. A 10 (2022) 13727–13734.
[56] P. Shen, P. Cao, Y. Yu, L. Wang, L. Zhao, L. Yang, Y. Lin, K. Xu, Carbon-Doped Nickle Via a Fast Decarbonization Route for Enhanced Hydrogen Oxidation Reaction in Alkaline Media, Small 19 (2023) 2303142.
[57] F. Zhou, X. Ke, Y. Chen, M. Zhao, Y. Yang, Y. Dong, C. Zou, Xa Chen, H. Jin, L. Zhang, S. Wang, Electron-distribution control via Pt/NC and MoC/NC dual junction: boosted hydrogen electro-oxidation and theoretical study, J. Energy Chem. 88 (2023) 513–520.